Chapter 12

# Impedance Matching Analysis of Cylindrical Plasmonic Nanoantennas Fed by Optical Transmission Lines

Karlo Queiroz da Costa, Janilson Leão Souza and Victor Dmitriev

Additional information is available at the end of the chapter

http://dx.doi.org/10.5772/67414

**Abstract**

An impedance matching analysis of two plasmonic nanocircuits connected to cylindrical nanoantennas is presented. In the first case, a bifilar optical transmission line (OTL) with finite length is connected between two nanodipoles, where one is illuminated by an optically focused Gaussian beam (receiving dipole) and the other radiates energy received from the OTL (emitting dipole). In the second case, the OTL is fed by a voltage source on one side and connected to a dipole-loop composed antenna on the other side. These circuits are analysed electromagnetically by the linear method of moments (MoM) with equivalent surface impedance of conductors. Some results are compared using the finite element method. The results show the impedance matching characteristics of the circuits as a function of their geometries and the broadband response of the second circuit due the broadband dipole-loop antenna.

**Keywords:** plasmonic circuits, cylindrical nanoantennas, impedance matching, broadband nanoantennas, method of moments (MoM)

## 1. Introduction

Nanophotonics is the study of optical systems in the nanometre scale [1]. A sub-area of nanophotonics is the nanoplasmonics, which analyses the interaction of optical fields with metal nanostructures [2]. With the development of nanoplasmonics, the concept of nanoantennas or optical antennas has emerged naturally as metal nanostructures that receive, transmit, localize and enhances optical fields [3–6]. This definition is similar to conventional RF-microwave

antennas, but the difference between these two regimes is that nanoantennas are not perfect conductors and we need to consider the finite conductivity of the metal. This characteristic leads to nanoantenna's size smaller than the wavelength of the incident wave. In other words, nanoantennas are electrically small resonant structures that can manipulate optical fields in small regions beyond the diffraction limit of light. This property of wavelength scaling for optical antennas is discussed in [7–9].

The research studies in nanoantenna field have increased mainly due to the development in modern nanofabrication techniques, such as the colloidal lithography, that is a bottom-up process, and the top-down processes like focused-ion beam (FIB) and electron-beam lithography (EBL) [10]. Some review papers on nanoantennas about theory, modelling, fabrication process and applications have been published [11–16].

The development in nanoantenna theory has also been increased due the important applications in different fields [17–28]. For example, the ability of metal nanoparticles to confine and enhance optical fields in nanometre regions is used in high-resolution microscopy, where fluorescence emission from a single molecule can be strongly enhanced [17–22]. Also, this radiation of a single emitter can be highly directed by nanoantenna arrays [23]. Other important applications are in nanobioimaging to analyse biological process [24], plasmonic photovoltaic cells [25], treatment of cancer in medicine [26], use of wireless at a nanoscale [27], plasmonic laser and optical data storage [28], and sub-wavelength integrated optical circuit [29]. In this work, we focus on the last application.

Examples of nanoantennas connected to plasmonic waveguide are presented in [29–31]. In this work, we make an alternative analysis and extend the results by using a different optical antenna with broadband characteristics. In particular, we consider two plasmonic nanocircuits connected to cylindrical nanoantennas. In the first circuit, a finite optical transmission line (OTL) is connected between two nanodipoles, where they are referred as receiving and emitting dipoles. In this circuit, the first dipole receives the energy from an optically focused Gaussian beam and delivers it to OTL, which connects to the second dipole to radiation. In the second circuit, the OTL is fed by a voltage source on one side and connected to a dipole-loop composed antenna on the other side. The analyses of these circuits are made by the linear method of moments (MoM) [32] with equivalent surface impedance of conductors [33]. We compare some results with the finite element method (FEM) [34]. The results show the impedance matching characteristics of the circuits as a function of their geometries, and the frequency response of the second circuit connected to the broadband dipole-loop antenna.

## 2. Theoretical model

In this section we present the geometries of the two nanocircuits, the linear method of moments (MoM) model used in the theoretical analysis, the Lorentz-Drude permittivity model and the equivalent surface impedance of the conductors, and the Gaussian beam used to feed the one circuit.

http://dx.doi.org/10.5772/67414

### 2.1. Nanocircuit geometries

The geometries of the analysed nanocircuits are presented in **Figures 1** and **2**. In the first case as given in **Figure 1**, the geometry is composed by an OTL, of length $L$ and radius $a_L$, and two nanodipoles. The receiving dipole 1 is illuminated by a Gaussian beam polarized along its axis, and the emitting dipole 2 radiates the energy received from the OTL. The arm length and radius of the dipoles 1 and 2 are $h_1$ and $a_{h1}$, and $h_2$ and $a_{h2}$, respectively.

In the second case as given in **Figure 2**, the circuit is composed by an OTL and one dipole-loop combined antenna. This circuit is fed on the left side by a voltage source of width $d$. The dipole is connected to OTL and the rectangular loop is above the circuit, where the OTL and dipole are on the plane $z = 0$ and the loop is on the plane $z = d_e$. The geometric parameters of the dipole-loop antenna (**Figure 2**) are $h_d$, $a_d$, $W_e$, $H_e$, $a_e$, $d_W$ and $d_H$, where the last two define the position of the loop with respect to the dipole.

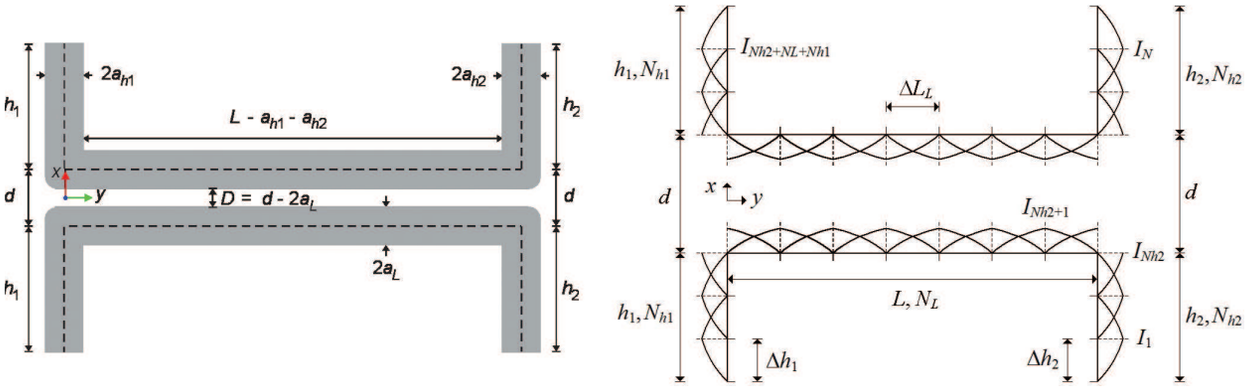


**Figure 1.** Left side: nanocircuit composed by OTL and two nanodipoles, where dipole 1 is illuminated by Gaussian beam and dipole 2 radiates energy of OTL. Right side: equivalent linear MoM model.

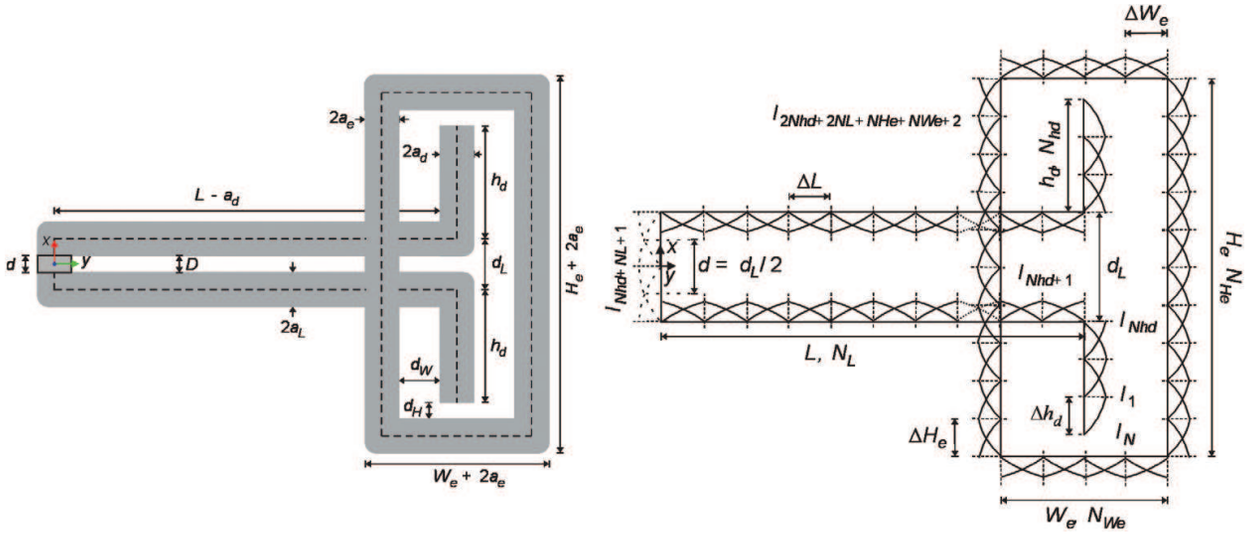


**Figure 2.** Left side: nanocircuit composed by OTL and one dipole-loop combined nanoantenna, where OTL is fed by a voltage source. Right side: equivalent linear MoM model.

In both circuits, the distance between the conductor's axis of OTL is $d$, in this case the distance between their surfaces is $D = d - 2a_L$. In these figures are also presented (right side) the equivalent linear MoM model used in the numerical analysis, which will be described in the next sections.

### 2.2. Method of moment model

There are different formulations of the linear approximation of MoM in the literature [32, 35–37]. Here we use the model given in Ref. [33], where the linear currents are expanded with sinusoidal basis functions. A brief description of this method is presented below, where we consider the scattering problem of **Figure 1** to explain the method.

In the scattering problem of **Figure 1**, the background medium is free-space and the conductors are in gold. The electrical permittivity of the gold conductors are represented by the Lorentz-Drude model $\varepsilon_1 = \varepsilon_0 \varepsilon_{r1}$ [1], where

$$\varepsilon_{r1} = \varepsilon_\infty - \frac{\omega_{p1}^2}{\omega^2 - j\Gamma\omega} + \frac{\omega_{p2}^2}{\omega_0^2 - \omega^2 + j\gamma\omega} \tag{1}$$

$\varepsilon_\infty = 8$, $\omega_{p1} = 13.8 \times 10^{15}$ s$^{-1}$, $\Gamma = 1.075 \times 1014$ s$^{-1}$, $\omega_0 = 2\pi c/\lambda_0$, $\lambda_0 = 450$ nm, $\omega_{p2} = 45 \times 10^{14}$ s$^{-1}$, and $\gamma = 9 \times 10^{14}$ s$^{-1}$. The losses of the metal are described by surface impedance $Z_s$. This surface impedance can be obtained approximately by considering cylindrical waveguide with mode $TM_{01}$ [33]:

$$Z_s = \frac{T J_0(Ta)}{2\pi a j\omega \varepsilon_1 J_1(Ta)} \tag{2}$$

where $T = k_0\sqrt{\varepsilon_{r1}}$ and $k_0 = \omega\sqrt{\mu_0 \varepsilon_0}$, $J_0$ and $J_1$ are the Bessel functions of first kind of order zero and one, respectively, $\omega$ is the operating angular frequency, $k_0$ is the propagation constant in air, $\mu_0$ is the magnetic permeability of air and $\varepsilon_0$ is the electrical permittivity of air.

The integral equation of the scattering problem is obtained by the boundary condition of tangential electric field at the surface's conductors $(\overline{E}_s + \overline{E}_i) \cdot \overline{a}_l = Z_s I$, where $\overline{a}_l$ is a unitary vector tangential to the surface of the metal, $\overline{E}_s$ is the scattered electric field due to the induced linear current $I$ on the conductor, $\overline{E}_i$ the incident electric field of the Gaussian beam source, or of the voltage source in the case of **Figure 2**, and $I$ is the induced longitudinal current in a given point of the nanocircuit. The scattered field is given by:

$$\overline{E}_s(\overline{r}) = \frac{1}{j\omega\varepsilon_0}\left[k_0^2 \int_l \overline{I} g(R)\, dl' + \int_l \frac{dI}{dl'} \nabla\, g(R)\, dl'\right] \tag{3}$$

where $g(R) = e^{-jk_0R}/4\pi R$ is the free-space Green's function, and $R = |\overline{r} - \overline{r}'|$ is the distance between source and observation points.

The numerical solution of the problem formulated by the boundary condition and Eqs. (1)–(3) is performed by linear MoM as follows. First, we discretize the linear circuit as shown in the right side of **Figure 1**, where $N_L$, $N_{h1}$ and $N_{h2}$ are the number of straight segments in $L$, $h_1$ and $h_2$, respectively. In the **Figure 1**, we have $N_L = 7$, $N_{h1} = N_{h2} = 3$. The discretization is uniform in $L$, $h_1$ and $h_2$, but the discretization length can be different, i.e. $\Delta L_L = L/N_L$, $\Delta h_1 = h_1/N_{h1}$ and

http://dx.doi.org/10.5772/67414

$\Delta h_2 = h_2/N_{h2}$. With this discretization, the total number of straight segments of the nanocircuit is $N_t = 2N_{h2}+2N_L+2N_{h1}$. For the method stability, we use the convergence conditions $\Delta h_2 > 2a_{h2}$, $\Delta h_1 > 2a_{h1}$, and $\Delta L_L > 2a_L$. Then the current in each segment is approximated by sinusoidal basis functions [33]. The expansion constants $I_n$ are shown in **Figure 1** where each constant defines one triangular sinusoidal current. To determine these constants, we use $N = N_t$ -2 rectangular pulse test functions with unitary amplitude and perform the conventional testing procedure. The following linear system of equations is obtained

$$V_m = Z_s I_m \Delta_m - \sum_{n=1}^{N} Z_{mn} I_n \tag{4}$$

where $m = 1, 2, 3, \ldots, N$, $Z_{mn}$ is the mutual impedance between sinusoidal current elements $m$ and $n$, $\Delta_m = [\Delta L_m+\Delta L_{m+1}]/2$ [32], and $V_m$ is the voltage induced in the segment $m$ due the source field $\overline{E}_i$. The solution of Eq. (4) produces the current along the nanocircuit. With these results, it is possible to calculate near- and far-field distributions and other parameters.

### 2.3. Gaussian beam source

In the case of nanocircuit 1 (**Figure 1**), the incident field is a Gaussian beam. This kind of wave is obtained by solving the scalar Helmholtz wave equation with the paraxial approximation [37]. The magnetic vector potential of a Gaussian beam polarized on the $x$-axis and travelling in the +$z$ direction is given by

$$\overline{A} = u_0 \sqrt{\frac{2}{\pi}} \frac{1}{w} \exp\left(\frac{-\rho^2}{w^2}\right) \exp\left[-j\left(\frac{k_0 \rho^2}{2R} - \phi\right)\right] e^{-jk_0 z}\, \overline{a}_x \tag{5}$$

where $u_0 = (2P\mu_0/k_0\omega)^{1/2}$, $P$ is the power of the beam, $w$ is the beam radius (**Figure 3**), $R$ is the curvature radius of the phase front and $\phi$ is the phase of the beam. The three principal parameters that define the beam are the power $P$, the radius of the beam waist $w_0$ (**Figure 3**) and the operating wavelength $\lambda$. With the vector potential given in Eq. (5), the $x$-component of electric field $E_x$ of the Gaussian beam can be obtained from the Maxwell equations [37].

The excitation beam used in **Figure 1** is focused on the receiving dipole 1 with polarization along the dipole axis ($x$-axis), the direction of propagation is +$z$, the beam axis is along the $z$-axis, and the minimum waist ($w_0$) is localized at $z = 0$, which is the plane of the nanocircuit. In all the analyses presented in this work for the nanocircuit 1 (**Figure 1**), we consider a fixed Gaussian beam with power, $P = 10^{-12}$ W, wavelength, $\lambda = 830$ nm and beam waist, $w_0 = 340$ nm. We use these values for comparisons with the results given in Ref. [29], but the analysis presented here can be applied for beams with other parameters. The field distribution of this beam is shown in **Figure 3**, where the electric field amplitude abs($E_x$) is presented on the $xz$ and $xy$ planes and the phase distribution angle of $E_x$ is presented on the $xz$ plane. The phase at $xy$ plane is constant.

## 3. Analysis of first nanocircuit

In this section, we analyse the first nanocircuit of **Figure 1**. In this case, we fix the Gaussian beam source given in **Figure 3** at $\lambda = 830$ nm, and analyse the impedance matching characteristic in function of the geometrical parameters of the OTL and nanodipoles.

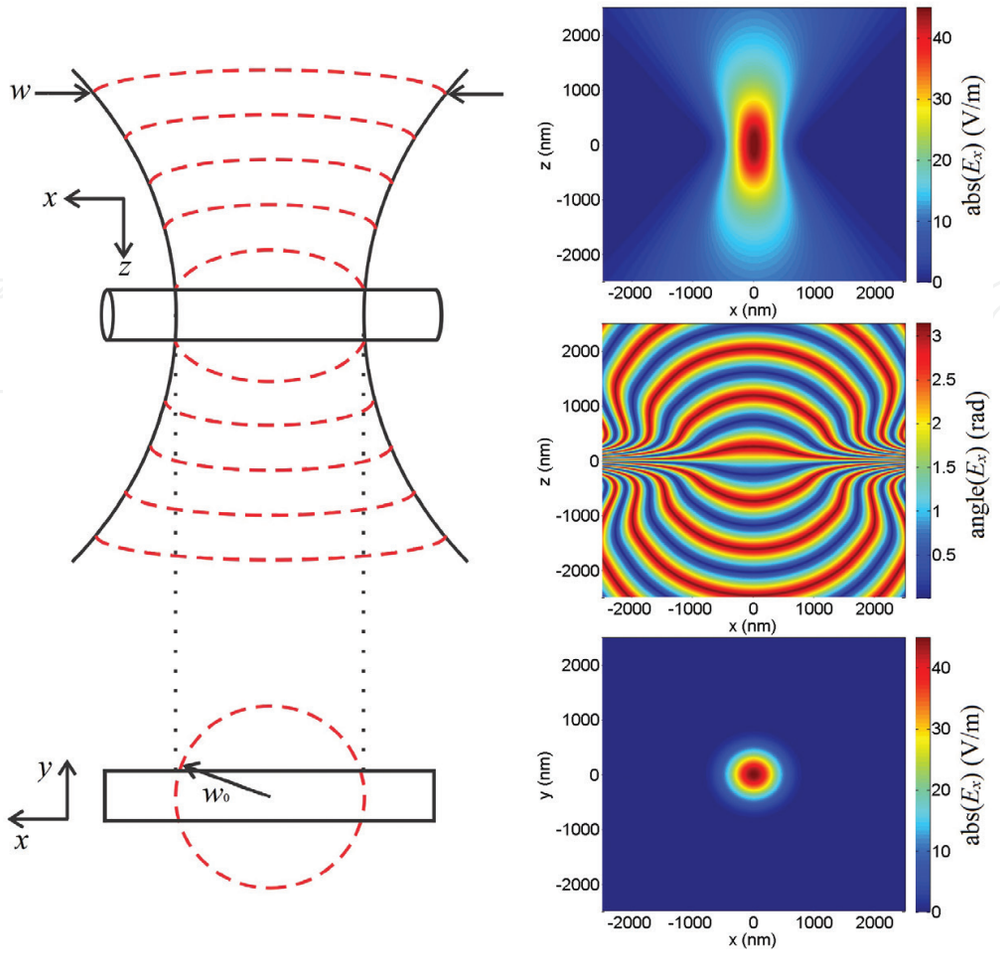


**Figure 3.** Field distribution of Gaussian beam with $P = 10^{-12}$ W, $\lambda = 830$ nm and beam waist $w_0 = 340$ nm at $xz$ and $xy$ planes.

### 3.1. Numerical example

Based on the theoretical model presented above, we developed a MoM code in Matlab to analyse the nanocircuit shown in **Figure 1**. In this sub-section, we present an example of simulation of the nanocircuit shown in **Figure 1** fed by the Gaussian beam depicted in **Figure 3**. **Figure 4** shows the geometry and discretization parameters used in this simulation and the result of the current distribution along the circuit. The near-field distribution for this example is given in **Figure 5**. Note that we use the total length of dipole as $H_1 = 2h_1+d$ and $H_2 = 2h_2+d$.

We observe in these results the stationary behaviour in the OTL, which is due to the mismatching in the impedances of nanodipole 2 and OTL. To make a quantitative measure of the impedance matching degree, we calculate approximately the voltage stationary wave ratio (*VSWR*) near nanodipole 2 as $VSWR = I_{max}/I_{min}$, where $I_{max}$ and $I_{min}$ are, respectively, the maximum and minimum current magnitude nearest to dipole 2. With this parameter, we calculate the voltage reflection coefficient as $|\Gamma_V| = (VSWR\text{-}1)/(VSWR\text{+}1)$. In this numerical example we obtained $|\Gamma_V| = 0.4$.

http://dx.doi.org/10.5772/67414

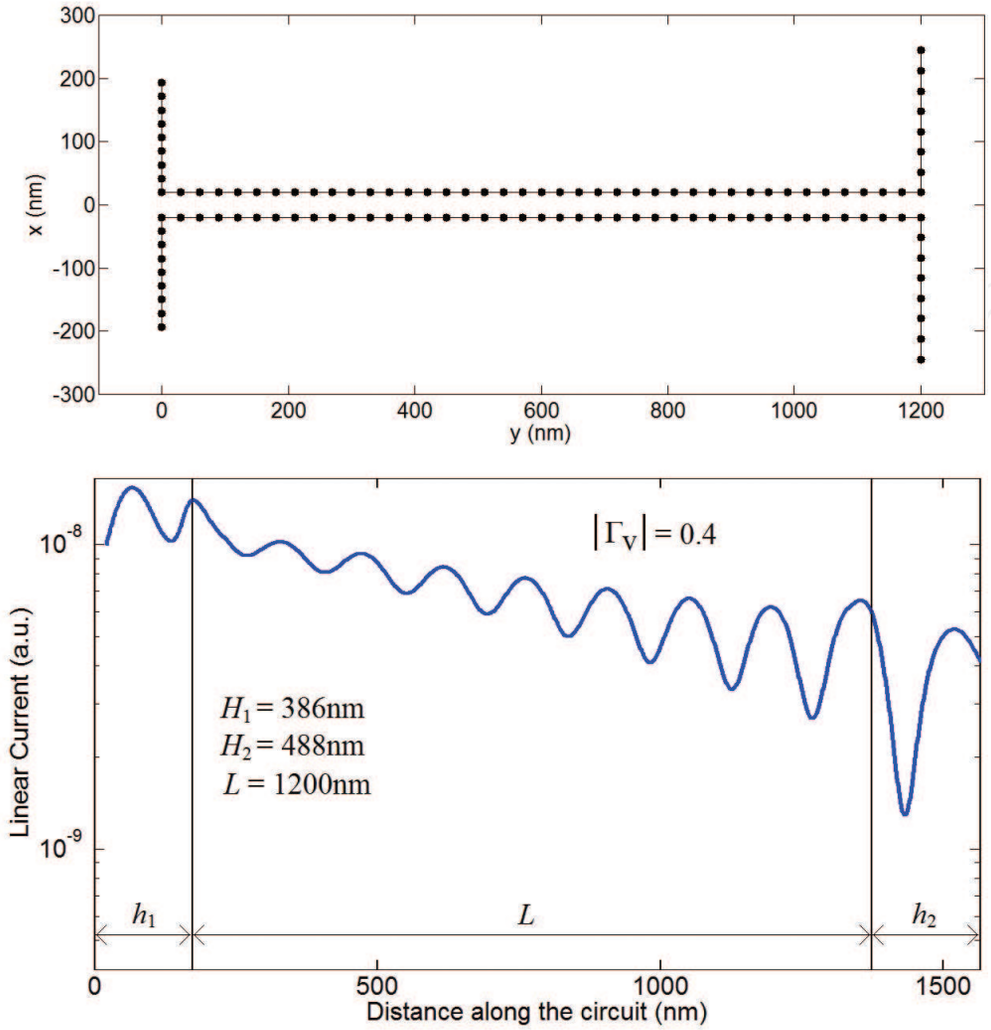


**Figure 4.** Up: geometry and discretization of nanocircuit with $H_1$ = 386 nm, $H_2$ = 488 nm, $L$ = 1200 nm, $a_{h1}$ = 10 nm, $a_L = a_{h2}$ = 15 nm, $D$ = 10 nm, $N_{h1}$ = 8, $N_{h2}$ = 7, $N_L$ = 40, $\Delta L_L$ = 30 nm, $\Delta h_1$ = 21.6 nm, $\Delta h_2$ = 32 nm and $N$ = 108. Down: amplitude of linear current distribution along nanocircuit. The voltage reflection coefficient of this circuit is $|\Gamma_V| = 0.4$.

### 3.2. Impedance matching analysis

This section presents a parametric analysis of the impedance matching of the nanocircuit for different values of $h_2$, $a_{h2}$, $a_L$ and $D$. In this analysis, we fixed the dimensions of the receiving dipole $h_1$ = 173 nm, $a_{h1}$ = 10 nm and the length of the OTL $L$ = 1200 nm. **Figure 6** presents the voltage reflection coefficient $|\Gamma_V|$ versus the total length of the emitting dipole $H_2 = 2h_2 + d$ for different values of $D$ = 10, 15 and 20 nm for the four cases ($a_L$ = 10 nm, $a_{h2}$ = 10 nm), ($a_L$ = 10 nm, $a_{h2}$ = 15 nm), ($a_L$ = 15 nm, $a_{h2}$ = 15 nm), and ($a_L$ = 15 nm, $a_{h2}$ = 20nm).

Analysing these curves we come to some conclusions. We note that the nanocircuits possess in general a smaller degree of input impedance matching (higher $|\Gamma_V|$) when the gap of the OTL $D$ is increased. The exceptions are the cases of **Figures 6a** and **b** in the range $H_2 < 400$ nm, where we have a better matching for higher $D$.

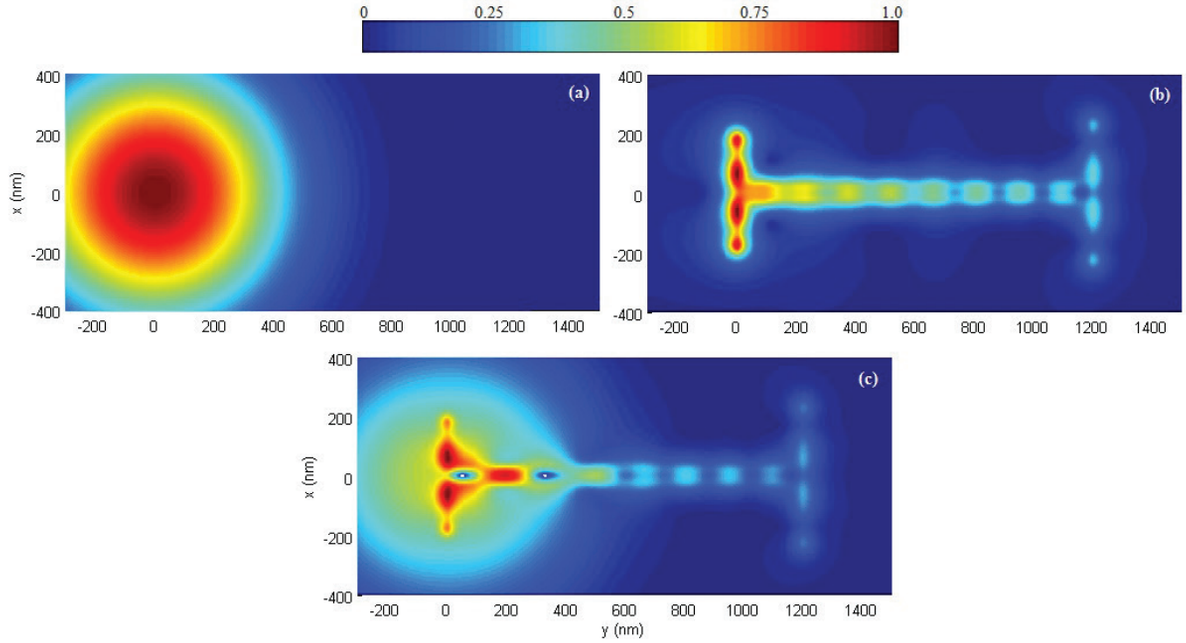


**Figure 5.** Normalized distribution of the electric field amplitude at plane $z$ = 30 nm: (a) incident field of the Gaussian beam abs($E_x^i$), (b) scattered field abs($E_x^s$), and (c) total field abs($E_x$).

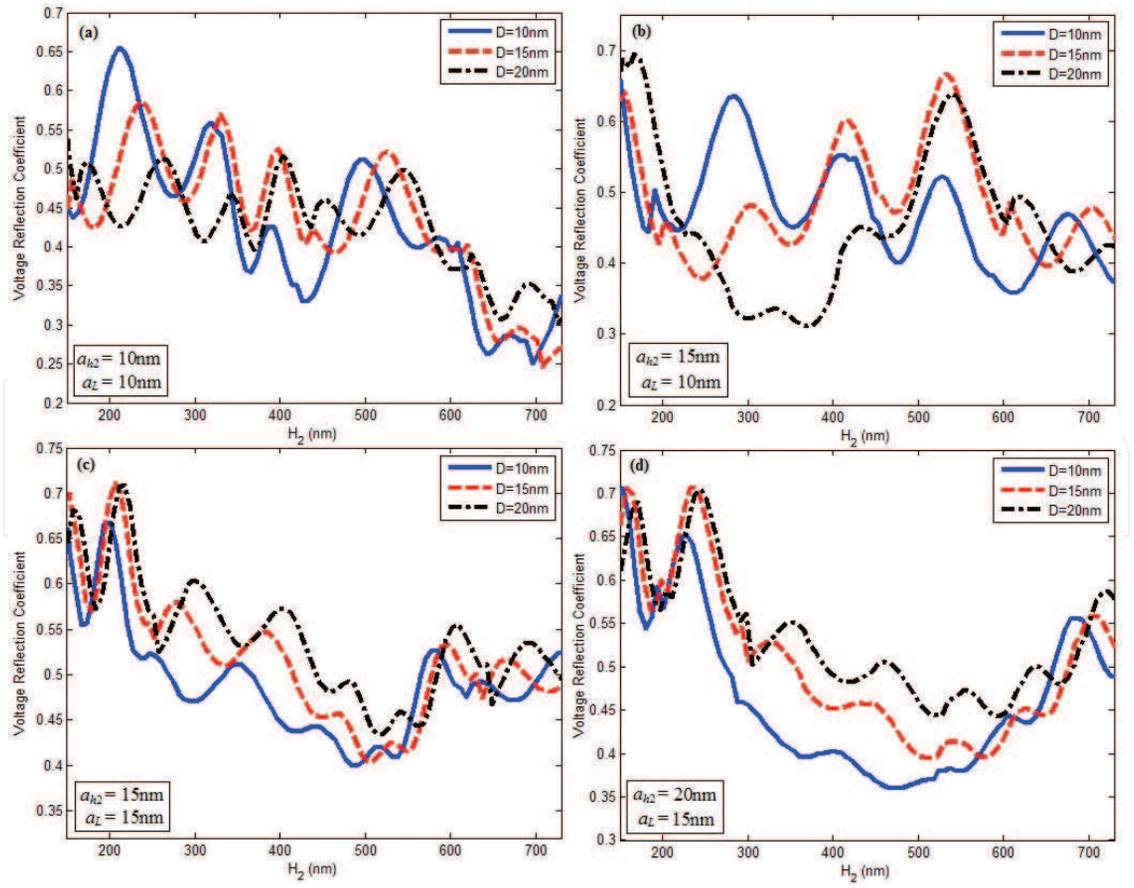


**Figure 6.** Voltage reflection versus $H_2 = 2h_2+d$ for different values of $D$ = 10, 15 and 20 nm. (a) $a_L$ = 10 nm and $a_{h2}$ = 10 nm, (b) $a_L$ = 10 nm and $a_{h2}$ = 15 nm, (c) $a_L$ = 15 nm and $a_{h2}$ = 15 nm, and (d) $a_L$ = 15 nm and $a_{h2}$ = 20 nm.

We also observe that in general the impedance matching is better when $a_{h2} > a_L$. This means that the values of $|\Gamma_V|$ in **Figure 6d** are smaller than those of **Figure 6c**, and the values of $|\Gamma_V|$ in **Figure 6b** are smaller than those of **Figure 6a**. The latter comparison is only true in the range of $H_2 < 400$ nm.

All these results show that we have many situations of good matching for different values of $D$, $a_L$, $a_{h2}$ and $H_2$. Min($|\Gamma_V|$) occurs for larger $H_2$, for examples in the cases $D$ = 10 nm and $H_2$ = 640 nm in **Figure 6a**, where $|\Gamma_V| \approx 0.26$, and $D$ = 10 nm and $H_2$ = 610 nm in **Figure 6b**, where $|\Gamma_V| \approx 0.35$. Other good results are for smaller $H_2$, for example the case of $D$ = 20 nm and $H_2$ = 300 nm in **Figure 6b**, where $|\Gamma_V| \approx 0.31$.

One way to choose the best geometric parameters of the circuit is to consider the case with better impedance matching and efficiency simultaneously. The efficiency of the circuit depends mainly on the attenuation of the current along the OTL, i.e. depends on the loss constant $\alpha$ of the OTL. This parameter is constant for the principal mode that propagates on the OTL, and can be obtained approximately by the average inclination of the current versus distance along the OTL. In equation form we have $\alpha = \Delta I/\Delta L$, where $\Delta I$ is the variation of the average amplitude of the current in decibels (dB) along a given distance $\Delta L$ (nm) in the OTL. With this definition the unit of this parameter is dB/nm. In the numerical example presented in **Figure 4** we have $\alpha \approx 0.007393$ dB/nm. This result is very close to $\alpha$ = 0.007296 dB/nm obtained in Ref. [29] where the OTL is similar to our case shown in **Figure 4** ($a_L$ = 15 nm and $D$ = 10 nm).

To understand better the behaviour of the impedance matching and efficiency characteristic of the results presented in **Figure 6**, we plot in **Figures 7** and **8** the current distributions for different geometric parameters. **Figure 7** shows the currents for two cases with same $a_L$ = 10 nm but different voltage reflection coefficients of $|\Gamma_V|$ = 0.31 and 0.67. In these results we observe a higher stationary wave for the case $|\Gamma_V|$ = 0.67 than for the case $|\Gamma_V|$ = 0.31. This shows that our approximate method to calculate $|\Gamma_V|$ provides a good measure of the degree of impedance matching. We also observe that the two cases present the same attenuation along the circuit (i.e. in both cases one has approximately the same loss constant $\alpha$ = 0.0111 dB/nm) because the OTL are constructed with the same radius of wires, $a_L$ = 10 nm.

**Figure 8** presents the current distribution for two cases with good impedance matching $|\Gamma_V|$ = 0.26 and 0.36, but with different loss constant of $\alpha$ = 0.0119 and 0.0084 dB/nm, respectively. This difference is mainly due to the difference of the radius $a_L$ of the OTL. For lower values of $a_L$ the attenuation is higher in OTL and this result is similar to that observed in RF-microwave regimes. This can be explained by the surface impedance model of Eq. (2), where smaller radius produces higher $Z_s$ and, consequently, higher loss in the conductors.

Another analysis of this circuit was done varying the dimensions of the receiving dipole 1 and fixing the dimensions of dipole 2 [32]. We observed that the dimensions of dipole 1 can modify the impedance matching and efficiency characteristics of circuit. The results show that good impedance matching does not necessarily mean a good efficiency in the receiving dipole, i.e. higher input current amplitude in dipole 1. For example, **Figure 9** presents the total electric field distribution at plane $z$ = 30 nm of two opposite situations. We can see in this

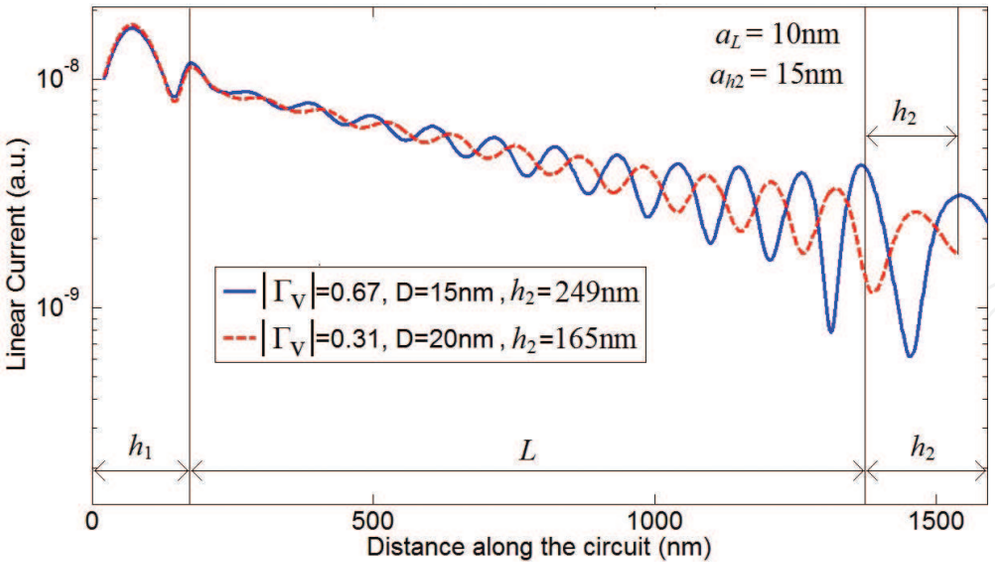


**Figure 7.** Current distributions of two circuits with the same values of $a_L$ = 10 nm possessing different voltage reflection coefficient ($|\Gamma_V|$ = 0.31 and 0.67).

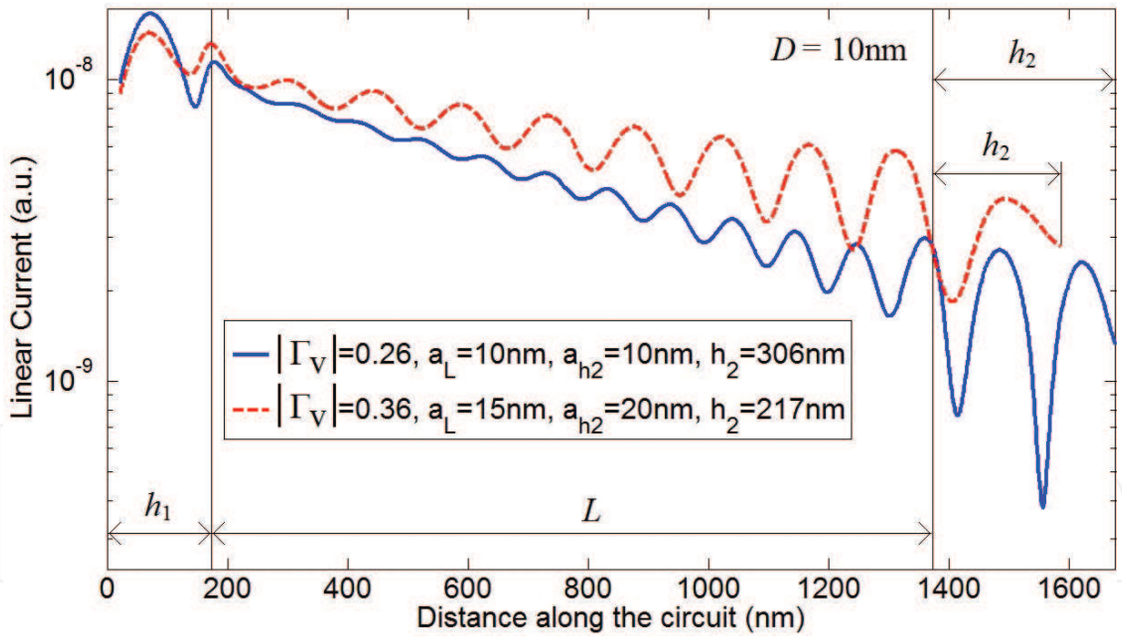


**Figure 8.** Current distributions of two nanocircuits with good voltage reflection coefficient ($|\Gamma_V|$ = 0.26 and 0.36) possessing different values of $a_L$.

figure the differences in the field intensity, showing higher values of the emitting dipole in the case when the dipole 1 operates in the first resonance (**Figure 9a**), i.e. this case presents better efficiency. However, the case of **Figure 9b** presents better impedance matching than the case of **Figure 9a**.

http://dx.doi.org/10.5772/67414

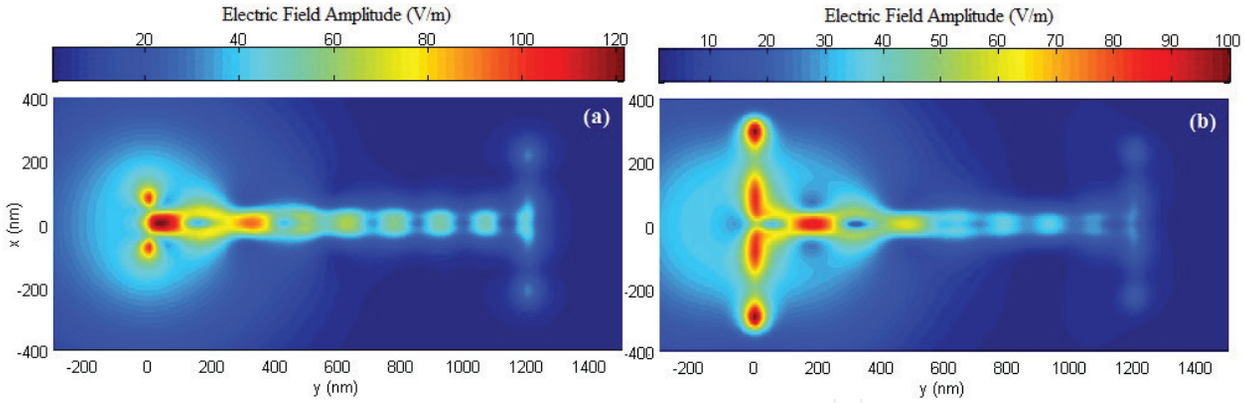


**Figure 9.** Total (scattered and incident) electric near-field distribution at plane $z$ = 30 nm (a) receiving dipole at first resonance with $H_1$ = 176.6 nm and $a_{h1}$ = 20 nm ($|\Gamma_V|$ = 0.42). (b) Receiving dipole at second resonance with $H_1$ = 637.7 nm and $a_{h1}$ = 20 nm ($|\Gamma_V|$ = 0.21). In these simulations, we fixed the following parameters of OTL and emitting dipole: $a_L$ =15 nm, $a_{h2}$ = 20 nm, $L$ = 1200 nm, and $N_L$ = 40.

## 4. Analysis of second nanocircuit

This section presents the analysis of second nanocircuit of **Figure 2**, where a voltage source fed an OTL on the left side and the other side is connected to a dipole-loop combined antenna. Due the broadband characteristic of this circuit, the analysis presents the spectral response of the circuit in the range of 100–400 THz for different values of the geometrical parameters (**Figure 2**). First, we analyse the isolated broadband dipole-loop antenna, and then we consider the OTL connected to this antenna.

### 4.1. Analysis of isolated dipole-loop

In this section, we analyse the isolated dipole-loop antenna and its spectral response. Note that this case without the OTL is obtained when $L$ = 0 in the nanocircuit given in **Figure 2**. To demonstrate the broadband characteristic of this nanoantenna, we first make a comparison with the conventional isolated nanodipole as a specific example. The geometrical parameters used in this example are: $h_d$ = 200 nm, $a_d$ = 20 nm, $d_L$ = 20 nm, $d_W$ = 50 nm, $d_H$ = 20 nm, $a_e$ = 20 nm, $W_e = 2a_e + 2a_d + 2d_W$, $H_e = 2h_d + d_L + 2a_e + 2d_H$ (**Figure 2**), $N_h$ = 5, $N_{He}$ = 13, $N_{We}$ = 4, $N_t$ = 46. Observe that the arm length of nanodipole is $h_d + a_d$ = 220 nm (**Figure 2**).

The first result obtained is the input impedance ($Z_{in} = R_{in} + jX_{in}$) presented in **Figure 10** for the case of isolated nanodipole (left) and dipole-loop antenna (right). This result is compared with the simulation by Comsol software, which is based on FEM. We observe that the two methods produce values with good agreement for the used frequency range. For the isolated dipole case, the first resonant frequency for the MoM is 191.9 THz and for the Comsol it is 187.7 THz, and the second resonant frequency for the MoM is 263.8 THz and for the Comsol it is 267.7 THz. In the case of dipole-loop antenna, it can be seen that the electromagnetic coupling between the dipole antenna and the loop antenna modifies the input impedance of the nanoantenna in comparison with the isolated dipole. It is further noted that the resonances

are moved to the lower frequencies. The first resonant frequency ($F_{\lambda/2}$) for the MoM is 185.1 THz and for the Comsol is 174.4 THz and the second resonant frequency ($F_{\lambda}$) for the MoM is 256.4 THz and for the Comsol is 254.7 THz.

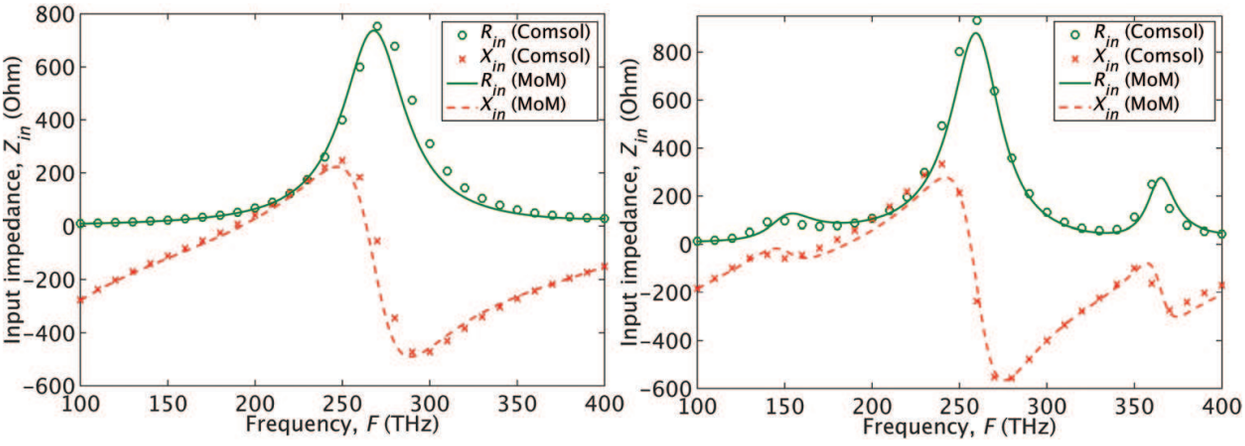


**Figure 10.** Input impedance of the isolated nanodipole (left) and dipole-loop antenna (right). The dimensions are: $h_d$ = 200 nm, $a_d$ = 20 nm, $d_L$ = 20 nm, $d_W$ = 50 nm, $d_H$ = 20 nm, $a_e$ = 20 nm.

**Figure 11** shows the results of calculation of the radiation efficiency and the reflection coefficient obtained by MoM and Comsol for the isolated nanodipole (left) and dipole-loop antenna. The reflection coefficient is given by $\Gamma = |(Z_{in}-Z_0)/(Z_{in}+Z_0)|$, where $Z_{in}$ is input impedance of the nanoantenna and $Z_0$ is the characteristic impedance of a given transmission line. The bandwidth is calculated by $B = 200[(F_s-F_i)/(F_s+F_i)]$, where $F_s$ is the upper frequency and $F_i$ is the lower frequency at the level -10 dB of the reflection coefficient.

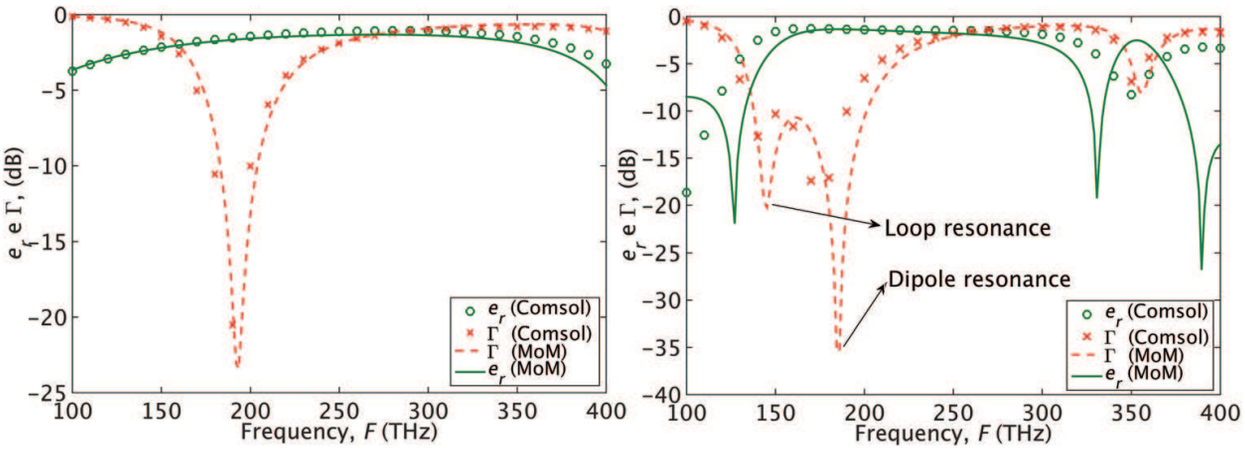


**Figure 11.** Radiation efficiency ($e_r$) and reflection coefficient (Γ) for nanodipole (left, $Z_0$ = 60 Ω) and dipole-loop antenna (right, $Z_0$ = 90 Ω) as function of frequency, calculated by MoM and Comsol.

For the isolated nanodipole (**Figure 11**, left), the maximum radiation efficiency calculated by the MoM and the Comsol are -1.06 and -1.32 dB, respectively, occurring around the second resonant frequency. However, the best input impedance matching point occurs around

http://dx.doi.org/10.5772/67414

the first resonant frequency, using $Z_0$ = 60 Ω. Therefore, the maximum efficiency and good impedance matching are found at different frequencies. This occurs because the characteristic impedance of an OTL is not necessarily matched to the input impedance of nanodipole with maximum efficiency [29]. The calculation of the reflection coefficient has been accomplished considering the connection of a line with $Z_0$ = 60 Ω, and for this impedance the final value obtained by the MoM was $B$ = 10.1% and by Comsol $B$ = 11.2%. The results of Γ show that the isolated dipole has a narrow bandwidth.

For the dipole-loop antenna (**Figure 11**, right), we can see that insertion of the loop besides modifying the input impedance also changes the reflection coefficient causing an increase of the bandwidth of the nanoantenna to 37.1% by MoM and 35.1% by Comsol. The increased bandwidth occurs because in the compound antenna occur an overlapping of different resonances of loop and dipole, which produces a greater bandwidth. We can also observe that the resonance of the loop (near $F \cong$ 145 THz) and the resonance of the dipole (near $F \cong$ 184 THz). In the frequency range between 150 and 280 THz, the radiation efficiency remains almost constant reaching the maximum value of -1.276 dB by the Comsol simulation and -1.35 dB for the MoM simulation. Thus we have a broadband antenna with high efficiency and with a possibility to achieve good impedance matching with an OTL of 90 Ω.

**Figure 12** shows the 3D far-field gain radiation pattern for the isolated dipole and the dipole-loop nanoantenna. The frequencies to which these diagrams were calculated correspond the bandwidth central frequencies ($F_c$ = ($F_s$ + $F_i$)/2) of **Figure 11**. The shape of these diagrams is approximately the same as of a small RF-microwave dipole. The maximum gain of the isolated dipole equals 1 for $F_c$ = 170.85 THz and the maximum gain of the composed antenna is equal to 1.4 for $F_c$ = 194.97 THz.

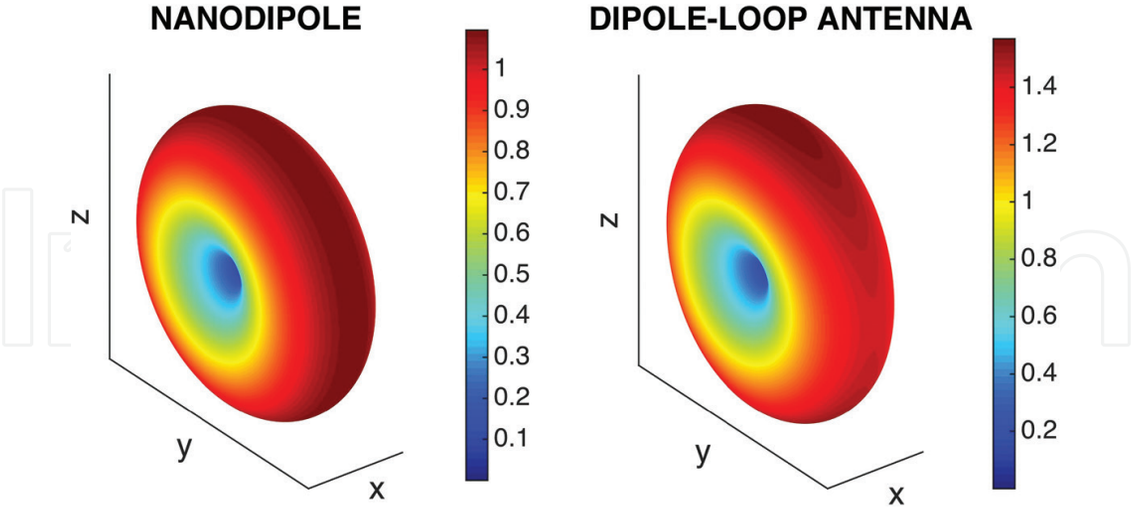


**Figure 12.** 3D far-field gain radiation pattern of the isolated dipole and composed antenna for the central frequencies 194.97 and 170.85 THz, respectively.

**Table 1** shows a parametric analysis of bandwidth of the composed nanoantenna for $d_W$ = 40, 50, 60 and 70 nm, and $d_H$ = 10 and 20 nm, respectively, varying only the parameters $d_W$ and $d_H$, and fixed parameters $h_d$ = 200 nm, $a_d$ = 20 nm, $d_L$ = 20 nm and $a_e$ = 20 nm. In this table are given the values

of the OTL impedance which maximize the bandwidth for each simulated. We can see from this parametric analysis that it is possible to optimize the bandwidth by adjusting the dimensions of the loop element. The best case obtained was for $d_H = 10$ nm and $d_W = 70$ nm, where $B = 42\%$.

| | | $d_W$ | | | | |
|---|---|---|---|---|---|---|
| | | **30 nm** | **40 nm** | **50 nm** | **60 nm** | **70 nm** |
| $d_H$ | 10 nm | $B = 35.4\%$ | $B = 36.8\%$ | $B = 38.3\%$ | $B = 40\%$ | $B = 42\%$ |
| | | $Z_0 = 85\ \Omega$ | $Z_0 = 105\ \Omega$ | $Z_0 = 100\ \Omega$ | $Z_0 = 115\ \Omega$ | $Z_0 = 120\ \Omega$ |
| | 20 nm | $B = 33.2\%$ | $B = 34.1\%$ | $B = 35.1\%$ | $B = 17.7\%$ | $B = 17.5\%$ |
| | | $Z_0 = 80\ \Omega$ | $Z_0 = 85\ \Omega$ | $Z_0 = 90\ \Omega$ | $Z_0 = 80\ \Omega$ | $Z_0 = 95\ \Omega$ |

**Table 1.** Results of parametric analysis of the composed nanoantenna.

### 4.2. Analysis of dipole-loop connected to OTL

In this section, we present the analysis of nanocircuit 2 of **Figure 2**. First, we present the variation of near- and far-field distribution in function of frequency, then the voltage reflection coefficient versus frequency is presented and finally a parametric analysis is presented.

#### *4.2.1. Near- and far-field results*

In this section, we present the variation of near and far-field distribution for a given example of nanocircuit as a function of frequency.

**Figure 13** shows the current distribution along the nanocircuit for the frequencies of 100, 200 and 300 THz, for the following parameters: $h_d = 200$ nm, $L = 1200$ nm, $a_d = a_L = a_e = 20$ nm, $d_L = 60$ nm, $d = d_L - 2a_L$, $d_e = 50$ nm, $d_W = 50$ nm, $d_H = 20$ nm, $N_h = 5$, $N_{We} = 4$, $N_{He} = 13$, $N_L = 29$ and $N_t = 104$. In the figure, the circle points identify the currents of each section of the nanocircuit. The points to the left of 1 and between 4 and 5 are the currents in the nanodipole, the ones between 1 and 2 and 3 and 4 are the currents of the OTL, those between 2 and 3 represent the current of the source, and finally those between 5 and 6, 6 and 7, 7 and 8 and to the right of 8 are the currents of the loop. We can see that while the frequency increases the attenuation of the current in the OTL increases, showing that at optical frequencies the conduction losses are higher. The stationary pattern presented in the figure shows the mismatch of the impedance of the optical transmission line and the nanodipole. The same oscillatory behaviour is observed in **Figure 14**, where the distribution of the normalized electric field near a parallel plane to the nanocircuit (for the same frequencies as in **Figure 13**) is shown. These fields were calculated for the plane $z = 80$ nm. It is evident that the energy transferred from the source to the nanodipole is reduced with the increasing frequency.

**Figure 15** shows the 3D far-field gain radiation diagram for this nanocircuit for $F = 100$, 200 and 300 THz. The shape of these diagrams can be explained when we pose that the nanocircuit in **Figure 2** acts as an array of two antennas spaced by the length $L$ of the OTL, wherein the first

http://dx.doi.org/10.5772/67414

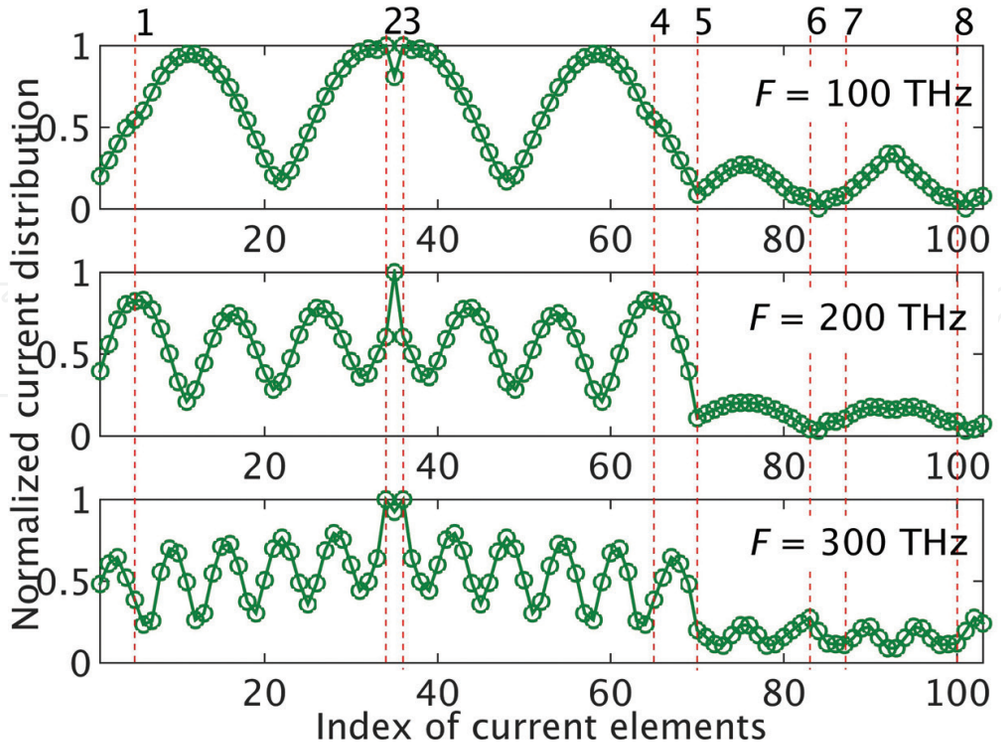


**Figure 13.** Normalized current distribution along the nanocircuit for $F$ = 100, 200 and 300 THz, with the parameters: $h_d$ = 200 nm, $L$ = 1200 nm, $a_d = a_L = a_e$ = 20 nm, $d_L$ = 60 nm, $d_e$ = 50 nm, $d_W$ = 50 nm, $d_H$ = 20 nm, $N_{hd}$ = 5, $N_{We}$ = 4, $N_{He}$ = 13, $N_L$ = 29 and $N_t$ =104.

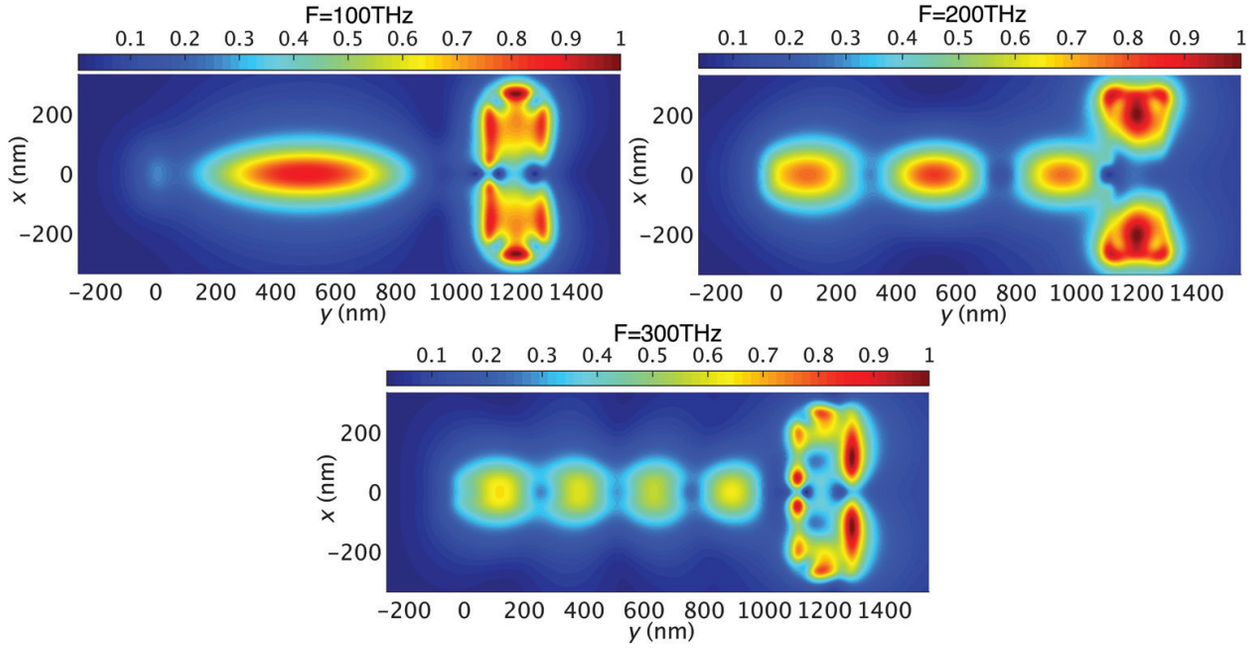


**Figure 14.** The electric field distribution in the plane $z$ = 80 nm, $F$ = 100 THz (top left), 200 THz (top right) and 300 THz (bottom), the parameters are: $h_d$ = 200 nm, $L$ = 1200 nm, $a_d = a_L = a_e$ = 20 nm, $d_L$ = 60 nm, $d_e$ = 50 nm, $d_W$ = 50 nm, $d_H$ = 20 nm, $N_{hd}$ = 5, $N_{We}$ = 4, $N_{He}$ = 13, $N_L$ = 29 and $N_t$ =104.

one is the dipole-loop antenna (right side of the circuit) and the second one is an equivalent dipole formed by the voltage source (left side of the circuit), that also radiates. Thus, the resulting radiation pattern of this arrangement is the product of the radiation pattern of one element and the array factor, leading to the shape drawn in **Figure 15**. Furthermore, it can be noted that when frequency is increased the resulting pattern has more side lobes. Another observation in these diagrams is that the radiation intensity is higher in the –*z* direction, because the loop element above the dipole acts as a reflector of waves in the downward direction.

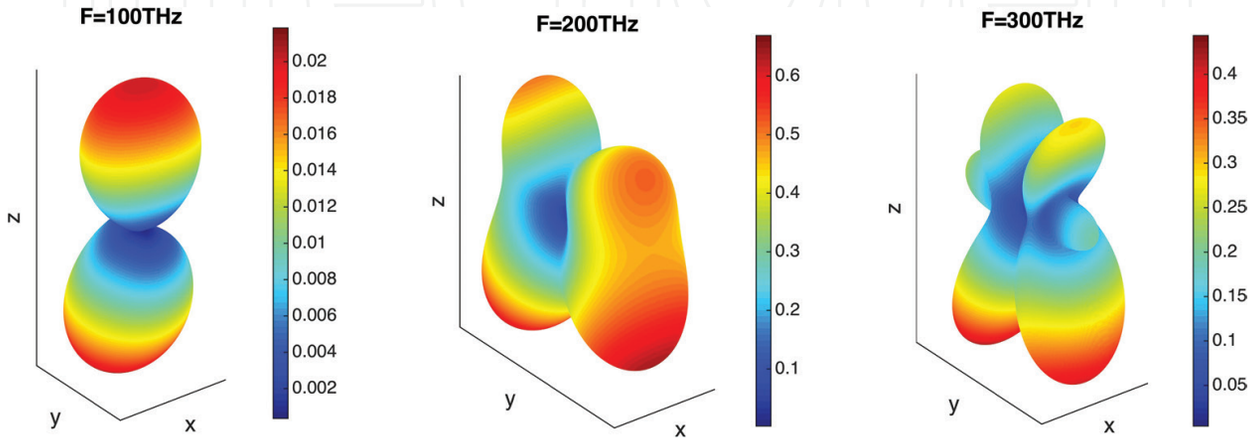


**Figure 15.** 3D far-field gain radiation pattern of the circuit for $F$ = 100, 200 and 300 THz.

### *4.2.2. Voltage reflection coefficient*

To analyse the impedance matching of the OTL with the antenna, it is necessary to calculate the voltage reflection coefficient as was done previously in Section 3.1. The results of calculations for the nanocircuit presented in **Figures 13** and **14** are shown in **Figure 16** for $|\Gamma_V|$ as a function of frequency for the nanocircuit with the loop and without it. In the figure, the minimum points $|\Gamma_V|$ are highlighted. They are -7.6 and -13.5 dB, at $F$ = 157.3 and 383.4 THz, respectively, for the case of the nanocircuit with the loop. This figure shows that the voltage reflection coefficient decreases with the addition of the loop into the optical nanocircuit near these frequencies (157.3 and 383.4 THz). Besides, this figure explains the stationary behaviour of the current and field shown in **Figures 13** and **14**.

For the frequencies corresponding to these minimum voltage reflection coefficients for the case of the nanocircuit with loop shown in **Figure 16**, the current distribution in **Figure 17** and normalized electrical field distribution in the plane $z$ = 80 nm in **Figure 18** are given.

It can be observed in **Figures 17** and **18** that with increasing of frequency the attenuation of the current and the electric field in the OTL increases due to conduction losses. It may be noted that for the frequency of 383.4 THz there is a significant drop at the standing wave rate in relation to the frequency of 157.3 THz, which presents a decrease in reflection losses on the line. On the other side, for the frequency 157.3 THz one has a higher level of current in OTL (higher transmission efficiency) than for the frequency 383.4 THz (**Figure 17**). This means, again, that a better impedance matching does not imply a higher transmission efficiency along the OTL.

http://dx.doi.org/10.5772/67414

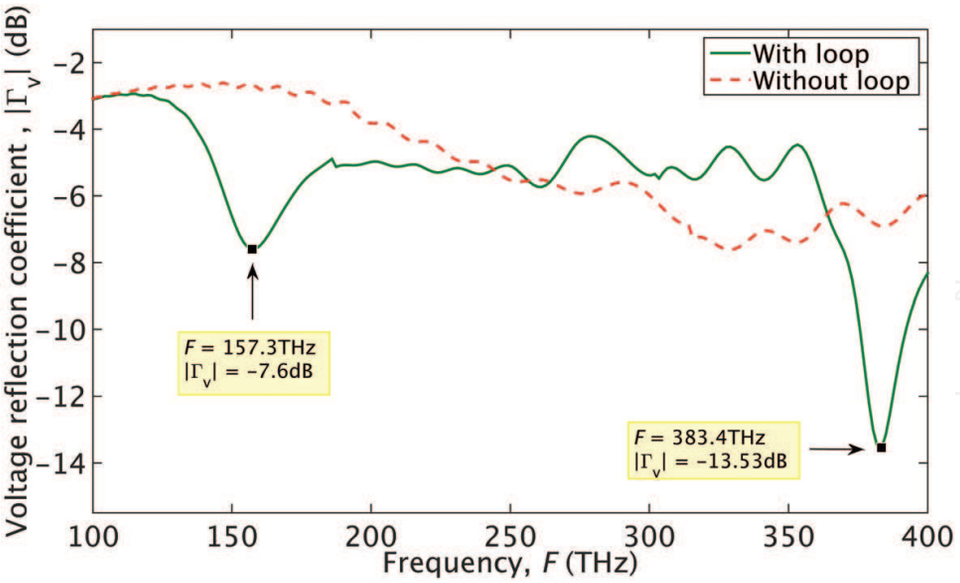


**Figure 16.** Voltage reflection coefficient as a function of frequency, the parameters are $h_d$ = 200 nm, $L$ = 1200 nm, $a_d$ = $a_L$ = $a_e$ = 20 nm, $d_L$ = 60 nm, $d_e$ = 50 nm, $d_W$ = 50 nm, $d_H$ = 20 nm, $N_{hd}$ = 5, $N_{We}$ = 4, $N_{He}$ = 13, $N_L$ = 29 and $N_t$ = 104.

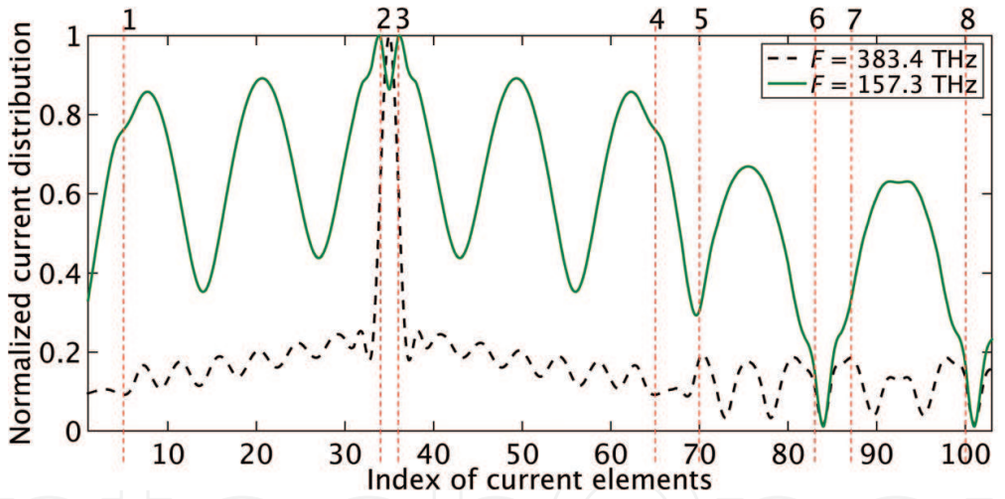


**Figure 17.** Current distribution for $F$ = 157.3 and 383.4 THz, with $|\Gamma_V|$ = -7.6 and -13.5 dB, respectively.

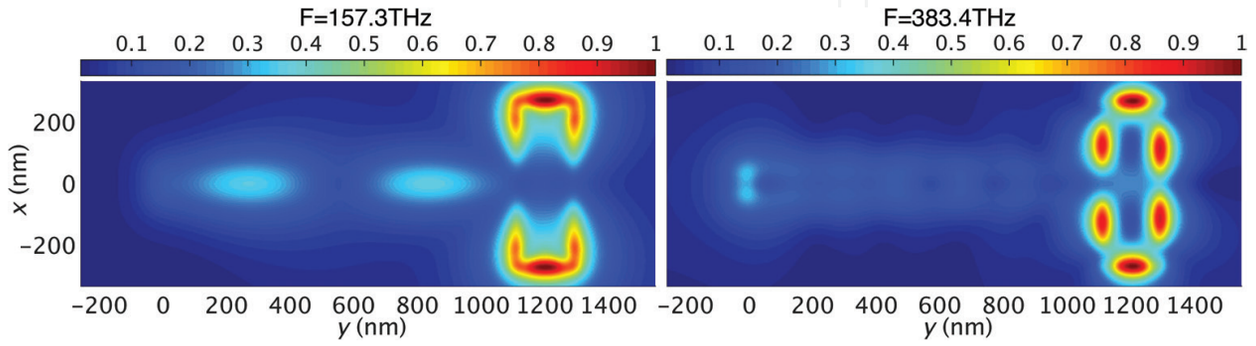


**Figure 18.** Electric field distribution in plane $z$ = 80 nm for frequencies $F$ = 157.3 (left) and 383.4 (right) THz, for cases with the reflection coefficient $|\Gamma_V|$ = -7.6 and -13.53 dB, respectively.

**Figure 19** shows the 3D far-field gain radiation pattern for the nanocircuit for $F$ = 157.3 and 383.4 THz. We observe again that the circuit in **Figure 2** works like an array of two dipoles spaced by the length $L$ of the OTL. Also, the gain level of case 157.3 THz is higher than that for 383.4 THz, which is in accordance with the current levels of **Figure 17**.

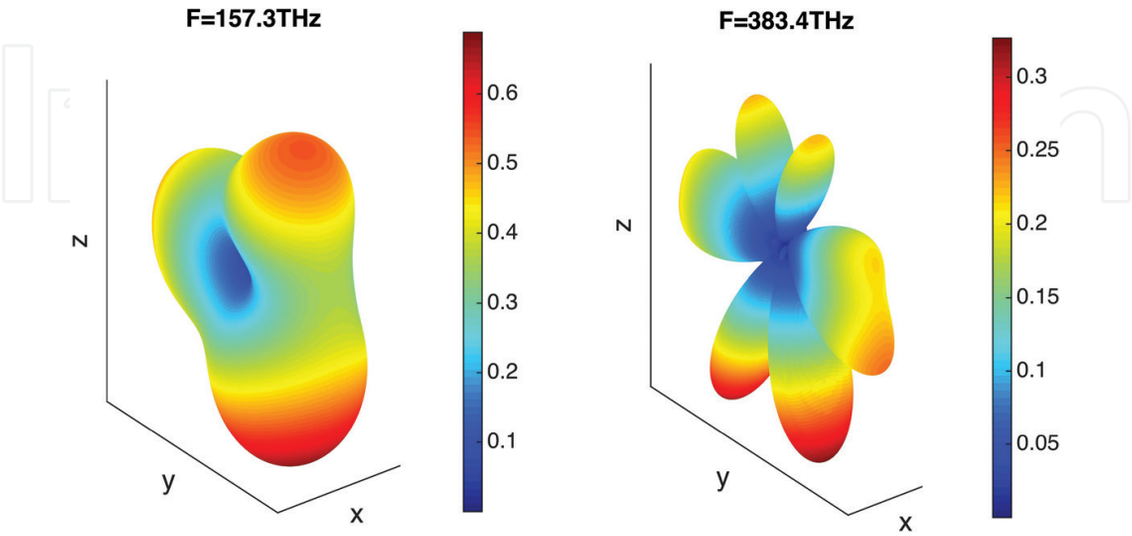


**Figure 19.** 3D far-field gain radiation pattern of the circuit for $F$ = 157.3 and 383.4 THz.

### *4.2.3. Parametric analysis*

Finally, a parametric analysis of the voltage reflection coefficient is shown in **Figure 20**. For the simulations we fix the following parameters: the distance between the surfaces of the OTL ($D$ = 20 nm), the length of the electric dipole ($h_d$ = 200 nm), the radii ($a_L$ = 20 nm, $a_d$ = 20 nm and $a_e$ = 20 nm) and the length of the OTL ($L$ = 1200 nm), and vary the parameters $d_W$ ($d_W$ = 30, 40 and 50 nm) and $d_H$ ($d_H$ = 10 and 20 nm), that consequently change the width ($W_e + 2a_e$) and the length ($H_e + 2a_e$) of the loop. In **Figure 20**, we show the results for the voltage reflection coefficient without the loop for comparison.

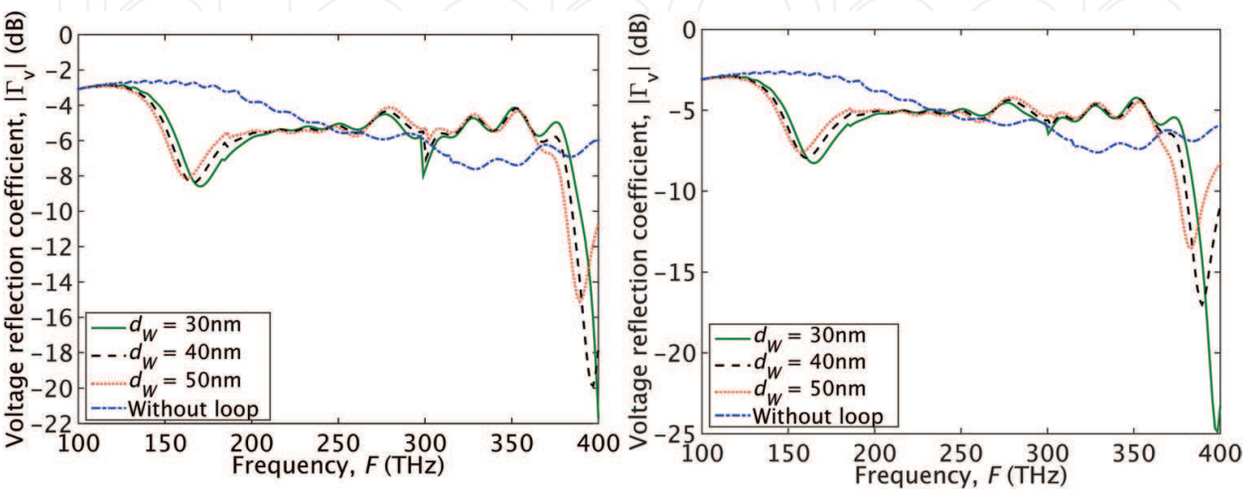


**Figure 20.** Voltage reflection coefficient ($|\Gamma_V|$) with the loop near the dipole for different values of $d_W$ (30, 40 and 50 nm) with $d_H$ = 10 (left) and 20 (right) nm and also $|\Gamma_V|$ without the loop.

http://dx.doi.org/10.5772/67414

Analysing these figures one comes to the following conclusions. In all simulated geometries of the circuit with the loop, there is an improvement in comparison with the circuit without the loop regarding impedance matching at some points as can be seen in the figures. The second conclusion is that, for smaller values of $d_W$, the curves of the voltage reflection coefficient ($|\Gamma_V|$) are shifted to the higher frequencies. This occurs because the impedance matching depends on the positions of the resonances of the nanoantenna, that are shifted to higher frequencies for smaller lengths of $d_W$. In general, the best impedance matching is obtained for smaller values of $d_W$. This behaviour can be explained by reduction of the reflection coefficient ($|\Gamma_V|$) of the nanoantenna when $d_W$ decreases. But then, an increase on $d_H$ results in increased values of $|\Gamma_V|$. This occurs because the reflection coefficient of nanoantenna increases with the increase on $d_H$.

## 5. Conclusions

An impedance matching analysis of two plasmonic nanocircuits with nanoantennas was presented. The first circuit is composed by an OTL connected between two nanodipoles, where one nanodipole is illuminated by a Gaussian beam. In the second circuit, a voltage source fed an OTL that is connected to a dipole-loop broadband nanoantenna. The linear MoM with finite surface impedance was used for numerical calculations, and some results were compared with FEM.

In the analysis of first circuit, we concluded that good impedance matching and transmission efficiency depends not only on the OTL and the emitting dipole, but also on the receiving dipole. In other words, the electromagnetic behaviour depends on the whole circuit. Also, we verified that good impedance matching does not imply on good transmission efficiency. An example of these opposite situations is presented in **Figure 9**.

In the second analysis, it was showed that a dipole-loop combined nanoantenna connected to an OTL can increase the operating bandwidth and improve the degree of impedance matching, when compared to the conventional isolated nanodipole. We obtained a best fractional bandwidth of 42%, for the dipole-loop nanoantenna, and a minimum voltage reflection coefficient of –25dB for this second nanocircuit.

## Author details

Karlo Queiroz da Costa[1]*, Janilson Leão Souza[1] and Victor Dmitriev[2]

*Address all correspondence to: karlo@ufpa.br

1 Federal Institute of Education, Science and Technology of Para, Tucuruí-PA, Brazil

2 Department of Electrical Engineering, Federal University of Para, Belém-PA, Brazil

## References

[1] Novotny L., Hecht B. Principles of Nano-Optics. 2nd ed. New York: Cambridge; 2012.

[2] Maier S. A. Plasmonics: Fundamentals and Applications. 1st ed. New York: Springer; 2007.

[3] Grober R. D., Schoelkopf R. J., Prober D. E. Optical antenna: towards a unity efficiency near-field optical probe. Appl. Phys. Lett. 1997;**70**(11):pp. 1354-1356.

[4] Pohl D. W. Near field optics seen as an antenna problem. In: Near Field Optics: Principles and Applications/The Second Asia-Pacific Workshop on Near Field Optics; October 20-23; Beijing, China. Singapore: World Scientific Publishing; 1999. pp. 9-21.

[5] Muhlschlegel P., Eisler H. J., Martin O. J. F., Hercht B., Pohl D. W. Resonant optical antenna. Science. 2005;**308**:pp. 1607-1608.

[6] Hecht B., Muhlschlegel P., Farahani J. N., Eisler H. J., Pohl D. W., Martin O. J. F., Biagioni P. Prospect of resonant optical antennas for nano-analysis. Chimia. 2006;**60**(11):pp. 765-769.

[7] Novotny L. Effective wavelength scaling for optical antennas. Phys. Rev. Lett. 2007;**98**:p. 266802.

[8] Bryant G. W., Abajo F. J. G., Aizpurua J. Mapping the plasmon resonances of metallic nanoantennas. Nano Lett. 2008;**8**(2):pp. 631-636.

[9] Weber D., Albella P., Gonzalez P. A., Neubrech F., Gui H., Nagao T., Hillenbrand R., Aizpurua J., Pucci A. Longitudinal and transverse coupling in infrared gold nanoantenna arrays: long range versus short range interactions regimes. Opt. Express. 2011;**19**(16):pp. 15047-15061.

[10] Giannini V., Dominguez A. I. F., Heck S. C., Maier S. A. Plasmonic nanoantennas: fundamentals and their use in controlling the radiative properties of nanoemitters. Chemical Rev. 2011;**111**(6):pp. 888-912.

[11] Bharadwaj P., Deutsch B., Novotny L. Optical antennas. Adv. Opt. Photonics. 2009;**1**:pp. 438-483.

[12] Novotny L., Hulst N. V. Antennas for light. Nat. Photonics. 2011;**5**:pp. 83-90.

[13] Lindquist N., Nagpal P., McPeak K. M., Norris D. J., Oh S. H. Engineering metallic nanostructures for plasmonics and nanophotonics. Rep. Prog. Phys. 2012;**75**:p. 036501.

[14] Biagione P., Huang J. S., Hecht B. Nanoantennas for visible and infrared radiation. Rep. Prog. Phys. 2012;**75**:p. 024402.

[15] Alu A., Engheta N. Theory, modeling and features of optical nanoantennas. IEEE Trans. Ant. Propag. 2013;**61**(4):pp. 1508-1517.

[16] Silveira G. N. M., Gabrielli L. H., Hasnain C. J. C., Figueroa H. E. H. Breakthroughs in photonics 2013: advances in nanoantennas. IEEE Phot. J. 2014;**6**(2):p. 0700706.

[17] Crozier K. B., Sundaramurthy A., Kino G, S., Quate C. F. Optical antennas: resonators for local field enhancement. J. Appl. Phys. 2003;**7**:pp. 4632-4642.

[18] Bharadwaj P., Novotny L. Spectral dependence of single molecule fluorescence enhancement. Opt. Express. 2007;**15**(21):pp. 14266-14274.

[19] Costa K. Q., Dmitriev V. Bowtie nanoantennas with polynomial sides in the excitation and emission regimes. Prog. Electro. Res. B. 2011;**32**:pp. 57-73.

[20] Taminiau T. H., Segerink F. B., Moerland R. J., Kuipers L., Hulst N. F. V. Near-field driving of a optical monopole antenna. J. Opt. A: Pure Appl. Opt. 2007;**9**:pp. S315–S321.

[21] Liaw J. W. Analysis of a bowtie nanoantenna for the enhancement of spontaneous emission. IEEE J. Sel. Top. Quantum Electron. 2008;**14**(6):pp. 1441-1447.

[22] Kinkhabwala A., Yu Z., Fan S., Avlasevich Y., Mullen K., Moerner W. E. Large single-molecule fluorescence enhancements produced by a bowtie nanoantenna. Nat. Phot. 2009;**3**:pp. 654-657.

[23] Taminiau T. H., Stefani F. D., Hulst N. F. V. Enhanced directional excitation and emission of single emitters by a nano-optical Yagi-Uda antenna. Opt. Express. 2008;**16**(14):pp. 16858-16866.

[24] Parajo M. F. G. Optical antennas focus in on biology. Nat. Phot. 2008;**2**:pp. 201-203.

[25] Atwater H. A., Polman A. Plasmonic for improved photovoltaic devices. Nat. Materials. 2010;**9**:pp. 205-213.

[26] Gupta D. D., Maltzahn G. V., Ghosh S., Bhatia S. N., Das S. K., Chakraborty S. Probing nanoantenna-directed photothermal destruction of tumors using noninvasive laser irradiation. App. Phys. Lett. 2009;**95**:p. 233701.

[27] Alu A., Engheta N. Wireless at the nanoscale: optical interconnects using matched nanoantennas. Phys. Rev. Lett. 2010;**104**(21):p. 213902.

[28] Cubukcu E., Yu N., Smythe E. J., Diehl L., Crozier K. B., Capasso F. Plasmonic laser antennas and related devices. IEEE J. Sel. Top. Quantum Electron. 2008;**14**(6):pp. 1448-1461.

[29] Huang J. S., Feichtner T., Biagione P., Hecht B. Impedance matching and emission properties of nanoantennas in an optical nanocircuit. Nano Lett. 2009;**9**(5):pp. 1897-1902.

[30] Wen J., Romanov S., Peschel U. Excitation of plasmonic gap waveguides by nanoantennas. Opt. Express. 2009;**17**(8):pp. 5925-5932.

[31] Costa K. Q., Dmitriev V., Souza J. L., Silvano G. Analysis of nanodipoles in optical nanocircuits fed by Gaussian beam. Int. J. Ant. Propag. 2014;**2014**:p. 429425.

[32] Costa K. Q., Dmitriev V. Simple and efficient computational method to analyze cylindrical plasmonic nanoantennas. Int. J. Ant. Propag. 2014;**2014**:p. 675036.

[33] Hanson G. W. On the applicability of the surface impedance integral equation for optical and near infrared copper dipole antennas. IEEE Trans. Ant. Propag. 2006;**54**(12):pp. 3677-3685.

[34] COMSOL Multiphysics 4.2a, COMSOL Inc. Available from: http://www.comsol.com./

[35] Sabaawi A. M. A., Tsimenidis C. C., Sharif B. S. Analysis and modeling of infrared solar rectennas. IEEE J. Sel. Top. Quantum Electron. 2013;**19**(3):p. 9000208.

[36] Rashidi A., Mosallaei H., Mittra R. Scattering analysis of plasmonic nanorod antennas: a novel numerically efficient computational scheme utilizing macro basis functions. J. Appl. Phys. 2011;**109**:p. 123109.

[37] Zhang K., Li D. Electromagnetic Theory for Microwaves and Optoelectronics. 2nd ed. New York: Springer; 2007.